

CENTRALIZED AND DECENTRALIZED SPACE OBJECT ESTIMATION AND DATA ASSOCIATION WITH PATTERN RECOGNITION

Steven A. Szklany*, John L. Crassidis[†], and Samuel S. Blackman[‡]

In this paper a decentralized orbital estimator is used to track multiple, clustered space objects from multiple observation sites. Decentralized estimation provides independent estimates from multiple sensors, rather than sending raw observables to a centralized node. Multiple estimates based on decentralized ground-based sensor information are fused via the covariance intersection method to provide a single estimate of the tracked spaced objects. Covariance intersection is a conservative approach, but provides consistent estimates, for fusing multiple estimates that share common states. When cross-covariance information is available in the covariance intersection algorithm, methods exist that provide optimal fusion. However, these methods will not generally provide estimates that match the centralized estimate since they incorporate only information that is posterior to the updates of the estimates being fused. For highly critical space object tracking, decentralized estimation provides redundancy in the event of a loss or failure of one of the independent sensors. The decentralized approach often yields a less accurate estimate of the object, considering the more conservative covariance that is created in the covariance intersection. Centralized estimation often provides a more accurate estimate of the observed space object but is unable to handle an outage of a contributing sensor. To address the accuracy differences between the centralized and decentralized cases, a robust approach for data association is developed. That approach couples gating methods for data association along with a star pattern recognition algorithm, called the planar triangular method, is developed. The planar triangular method has been shown to work effectively for spacecraft attitude determination using star trackers by comparing stars in field-of-view to those present in the catalog.

This work shows the effectiveness of combining traditional data association methods with an existing planar triangle pattern recognition algorithm for space object data association in both the centralized and decentralized estimation cases. Results indicate that the traditional gating algorithm significantly improves the planar triangular methods accuracy for space object data association of closely-spaced clutters in highly uncertain environments. The robustness of the gating-assisted planar triangle method for data association overcomes the loss of precision experienced using decentralized orbit estimation thus providing nearly identical data association performance as the centralized estimation solution.

INTRODUCTION

Space Situational Awareness (SSA) deals with collecting and maintaining knowledge of all objects orbiting the Earth. It is defined as the comprehensive knowledge of space objects and the

*Graduate Student, University at Buffalo, State University of New York, Amherst, NY 14260, Department of Mechanical & Aerospace Engineering. Email: sszklany@buffalo.edu.

[†]Samuel P. Capen Chair Professor, University at Buffalo, State University of New York, Amherst, NY 14260, Department of Mechanical & Aerospace Engineering. Email: johnc@buffalo.edu. Fellow AAS.

[‡]Retired, Raytheon, Email: samuelblackman56@gmail.com.

ability to track, understand and predict their future location. The orbits in space are comprised of functional and defunct objects, as well as artificial objects. Functional objects are actively controlled so that their attitude and position can be maintained to accomplish mission objectives. However, defunct objects generally are not actively controlled for attitude and positional corrections. Generally these objects do not follow pure Keplerian motion, being subjected to drift and decay. Uncontrolled objects pose a difficult problem in maintaining adequate SSA.

A common topic associated with Resident Space Objects (RSOs) is *Kessler's syndrome*, which theorizes that creation of new debris occurs faster than the time taken by natural forces to remove them. As space object density increases, the collision between objects could cause a cascading effect, i.e. each collision generates more debris and thereby increases the likelihood of further collisions. There are more than 21,000 piece of debris with a radius larger than 10 centimeters. The increasing number of objects to be tracked in space is straining the sensors and algorithms which track those objects which puts many critical space missions at risk for collisions or impacts by a space object.

The primary step in resolving the ever growing issue of space debris is proper association and identification of RSOs. Typically, RSOs are identified by matching sensor measurements (e.g. space-surveillance telescope data) to a space object catalog of previously identified objects. If the current RSO cannot be matched with any cataloged object, then that object is deemed an unidentified object, otherwise known as an “uncorrelated track,” which is placed in the catalog and monitored throughout its entire life span if possible. A catalog is simply a directory of objects that includes information pertaining to the object’s estimated position and characteristics, such as the ballistic coefficient-like term found in two-line elements. The process of matching sensor measurements to a target, or RSO, is known as data association. Data association is fundamental in determining which RSOs within a sensor’s field-of-view (FOV) are cataloged, and which are previously unidentified objects. An accurate and up-to-date RSO catalog is critical in avoidance maneuver planning and overall SSA.¹

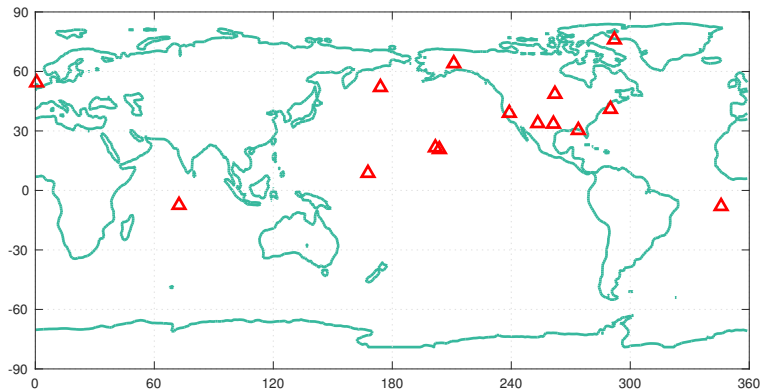


Figure 1. Locations of US Space Surveillance Network Sensors²

The creation of more observation sites improves the likelihood of observing and tracking more objects in space, but presents new problems by way of data fusion. The data collected by multiple sites needs to be appropriately fused in order to provide highly accurate estimates of the object.

Figure 1 illustrates the spread of space surveillance network sites across the world. Although this is only a portion of all the space observing sensors in the world, it is clear that multiple observation sites improve coverage to the space surveillance network.

Much work has been done in the area of identification and data association in the recent years. These can be broadly divided into Gaussian and non-Gaussian methods. A covariance-based track association approach is shown in Ref. 3. An entropy-based data association approach for non-Gaussian probability density functions (pdfs) is shown in Ref. 4. Tracking multiple number of objects using finite-set statistics and finite mixture-model representations of multi-object pdfs is developed in Ref. 5. A Gaussian mixture Probability Hypothesis Density filter for multiple space object tracking is presented in Ref. 6. The ∂ -General Labeled Multi-Bernoulli filter has been studied for tracking a large number of objects in Ref. 7. The use of magnetometers in identifying space objects in geosynchronous orbits has been studied and discussed in Ref. 8. Each of the aforementioned algorithms has its advantages and disadvantages. For example, Gaussian-based approaches may not work well when the pdf is non-Gaussian, and non-Gaussian approaches may be computationally expensive and also overburdensome when Gaussian pdfs exist.

Decentralized orbit determination provides many logistical benefits in highly critical tracking applications. In multitarget-multisensor applications, decentralized estimation provides redundancy to the targets being tracked. That redundancy is valuable in multiple optical sensor applications where weather patterns could be influencing one or more of the sensor sites. In addition to weather events, communication outages and sensor malfunctions are likely scenarios in complex multisensor optical tracking applications. In a centralized application, the loss of a single sensor will significantly impact the tracking mission.

Data association is the process of matching an unknown measured object to its known truth. Problems attributed to associating the true object from a cluster of similar objects can be addressed by various methods. These problems have been very well studied for the case of target tracking and multiple target tracking.⁹ Data association has been studied in detail for target tracking in surveillance systems employing one or more sensors. In particular, many algorithms such as nearest neighbor, global nearest neighbor, multiple hypothesis tracking, joint probabilistic data association have been extensively studied.⁹ Coupling traditional data association techniques with other methods for SSA is the focus of this work. In this paper traditional data association methods, such as elliptical/validation gates, are used to improve the association of the RSO when combined with a star pattern recognition-based approach, called the Planar Triangle Method (PTM).¹⁰ The challenge of this work is overcoming the errors in the RSO cataloged position which significantly contribute to the overall uncertainty of the observation-to-truth correlation.

The outline of this paper proceeds as follows. First, the dynamics and measurement models are reviewed. Then, the PTM and orbit determination algorithms are discussed. The decentralized data fusion solution is presented as the covariance intersection approach next. The following section includes traditional data association methods are covered which includes the optimal assignment problem. Further discussion is included to describe the combination of the elliptical gating data association with the planar triangle method. Next, simulation results are presented for highly cluttered environments for centralized and decentralized orbit estimations. Finally, conclusions are drawn upon the simulation results.

DYNAMICS AND MEASUREMENT MODELS

This section briefly covers the dynamics model, as well as the focal-plane sensor model used for telescopes. A derivation of the errors induced on the focal-plane measurements due to estimation errors is also shown. There are many forces acting on a space object that perturb it away from the nominal orbit. These perturbations, or variations in the orbital elements, can be classified based on how they affect the Keplerian elements. The three basic type of orbital perturbations are secular variations, short period variations and long period variations. Secular variations have a long term linear variation on the orbit prediction, they cause the orbital elements to increase or decrease as time progresses. The main types of perturbation faced by a body in space are third-body perturbations, atmospheric drag, J_2 perturbations, solar radiation pressure, etc. Here, only J_2 and atmospheric drag perturbations are considered. The gravity potential for an arbitrary body is expressed as¹¹

$$V(r, \phi) = -\frac{Gm}{r} \left[1 - \sum_{k=2}^{\infty} \left(\frac{r_{\text{eq}}}{r} \right)^k J_k P_k(\sin \phi) \right] \quad (1)$$

where G is gravitational constant, m is mass of the body, r_{eq} is the equatorial radius of the body, r is the distance to a point away from the body, J_k is the k^{th} zonal gravitational harmonic, P_k is the k^{th} order Legendre polynomial, and ϕ is the elevation angle of the vector tracking a point away from the body. The perturbing acceleration due to J_2 harmonics is given by

$$\mathbf{a}_{J_2} = -\frac{3}{2} J_2 \left(\frac{\mu_g}{r^2} \right) \left(\frac{r_{\text{eq}}}{r} \right)^2 \begin{pmatrix} \left(1 - 5 \left(\frac{z}{r} \right)^2 \right) \frac{x}{r} \\ \left(1 - 5 \left(\frac{z}{r} \right)^2 \right) \frac{y}{r} \\ \left(3 - 5 \left(\frac{z}{r} \right)^2 \right) \frac{z}{r} \end{pmatrix} \quad (2)$$

The atmospheric drag perturbation is given by

$$\mathbf{a}_D = \frac{1}{2} \frac{C_D A}{m} \rho_0 R_{\oplus} v^2 \quad (3)$$

The atmospheric drag coefficients have been condensed in Two Line Element (TLE) sets. The TLE sets contain a parameter B^* which represents critical coefficients of a tracked items atmospheric drag terms. The value B^* is given by¹²

$$B^* = \frac{1}{2} \frac{C_D A}{m} \rho_0 R_{\oplus} \quad (4)$$

where C_D is the drag coefficient, A is the cross-sectional area, m is the mass, ρ_0 is the atmospheric density at perigee, and R_{\oplus} is the Earth radius. The ballistic coefficient, B is related to B^* by

$$B = \frac{R_{\oplus} \rho_0}{2B^*} \quad (5)$$

The dynamics model for the i^{th} RSO is given by

$$\ddot{\mathbf{r}}_i^{\text{RSO}} = -\frac{\mu}{r_i^3} \mathbf{r}_i^{\text{RSO}} + \mathbf{a}_{J_2i} + \mathbf{a}_{Di} \quad (6)$$

where $\mu = Gm$, $\mathbf{r}_i^{\text{RSO}} = [x_i \ y_i \ z_i]^T$ and $r_i = \|\mathbf{r}_i^{\text{RSO}}\|$.

Unit vector observations are assumed here. Focal-plane detectors form measurements according to a set of *collinearity equations*, which are standard in many photogrammetry applications.¹³ Assuming that the camera boresight is aligned with the z -axis, these are given by

$$\alpha_i = -f \frac{A_{11}(x_i - X) + A_{12}(y_i - Y) + A_{13}(z_i - Z)}{A_{31}(x_i - X) + A_{32}(y_i - Y) + A_{33}(z_i - Z)}, \quad i = 1, 2, \dots, N \quad (7a)$$

$$\beta_i = -f \frac{A_{21}(x_i - X) + A_{22}(y_i - Y) + A_{23}(z_i - Z)}{A_{31}(x_i - X) + A_{32}(y_i - Y) + A_{33}(z_i - Z)}, \quad i = 1, 2, \dots, N \quad (7b)$$

where f is the focal length, (X, Y, Z) is the sensor (instrument) coordinates, denoted in vector form by $\mathbf{r}^{\text{INSTR}} = [X \ Y \ Z]^T$, and A_{ij} are the elements of the attitude matrix, which is a proper orthogonal 3×3 matrix, denoted by A . This matrix is given by three successive rotations, given by

$$A = A_{\mathcal{T}/\mathcal{U}} A_{\mathcal{U}/\mathcal{F}} A_{\mathcal{F}/\mathcal{I}} \quad (8)$$

where \mathcal{T} denotes the Instrument (INSTR) coordinate system, \mathcal{U} denotes the local East-North-Up (ENU) coordinate system, \mathcal{F} denotes Earth-Centered Earth-Fixed (ECEF) coordinate system, and \mathcal{I} Earth-Centered Inertial (ECI) coordinate system. The ENU coordinate system is formed by a plane tangent to Earth's surface at a specific location. The origin of the tangent plane is usually dictated by the geolocation of a radar, telescope, or other instrument. Conversions between the various frames can be found in Ref. 2.

The observation vector that is directly measured by the instrument is

$$\boldsymbol{\gamma}_i \equiv \begin{bmatrix} \alpha_i \\ \beta_i \end{bmatrix} \quad (9)$$

and the corresponding measurement equation with noise is

$$\tilde{\boldsymbol{\gamma}}_i = \boldsymbol{\gamma}_i + \mathbf{w}_i \quad (10)$$

The zero-mean Gaussian noise process \mathbf{w}_i is assumed to have covariance given by

$$R_i^{\text{FOCAL}} = \frac{\sigma^2}{1 + d(\alpha_i^2 + \beta_i^2)} \begin{bmatrix} (1 + d\alpha_i^2)^2 & (d\alpha_i\beta_i)^2 \\ (d\alpha_i\beta_i)^2 & (1 + d\beta_i^2)^2 \end{bmatrix} \quad (11)$$

where d is on the order of one (and often simply set to one) and σ is assumed to be known.¹⁴

In unit vector form, the observations are

$$\mathbf{b}_i = A \mathbf{r}_i, \quad i = 1, 2, \dots, N \quad (12)$$

where

$$\mathbf{b}_i \equiv \frac{1}{\sqrt{f + \alpha_i^2 + \beta_i^2}} \begin{bmatrix} -\alpha_i \\ -\beta_i \\ f \end{bmatrix} \quad (13a)$$

$$\mathbf{r}_i \equiv \frac{1}{\sqrt{(x_i - X)^2 + (y_i - Y)^2 + (z_i - Z)^2}} \begin{bmatrix} x_i - X \\ y_i - Y \\ z_i - Z \end{bmatrix} \quad (13b)$$

The measurement equation for the unit vector is

$$\tilde{\mathbf{b}}_i = \mathbf{b}_i + \mathbf{v}_i, \quad \mathbf{v}_i^T \mathbf{b}_i = 0 \quad (14)$$

where the statistics of the noise \mathbf{v}_i are given by

$$\mathbb{E}\{\mathbf{v}_i\} = \mathbf{0} \quad (15a)$$

$$R_i^{\text{QUEST}} \equiv \mathbb{E}\{\mathbf{v}_i \mathbf{v}_i^T\} = \sigma^2 (I_{3 \times 3} - \mathbf{b}_i \mathbf{b}_i^T) \quad (15b)$$

where $I_{3 \times 3}$ is a 3×3 identity matrix. The QUEST measurement model¹⁵ of Eq. (15b) makes the generally reasonable assumption that the uncertainty in the line-of-sight (LOS) unit vector measurement lies in the tangent plane to the unit sphere at the point where it intersects the measurement. This assumption becomes less valid for sensors with a wide FOV and LOS vectors far from the boresight direction.

To derive a wide-FOV covariance model, the 2×2 covariance R_i^{FOCAL} from Eq. (11) is transformed to a rank-deficient 3×3 covariance matrix (R_i^{wFOV}) via the Jacobian:¹⁶

$$J_i \equiv \frac{\partial \mathbf{b}_i}{\partial \gamma_i} = \frac{1}{\sqrt{f + \alpha_i^2 + \beta_i^2}} \begin{bmatrix} -1 & 0 \\ 0 & -1 \\ 0 & 0 \end{bmatrix} - \frac{1}{f + \alpha_i^2 + \beta_i^2} \mathbf{b}_i [\alpha_i \quad \beta_i] \quad (16)$$

With this J_i , the new covariance is given by

$$R_i^{\text{wFOV}} = J_i R_i^{\text{FOCAL}} J_i^T \quad (17)$$

Note that Ref. 16 calls this covariance R_i^{NEW} . As this covariance is no longer a “new” result, the notation R_i^{wFOV} is adopted. Reference 17 proves that the wide-FOV covariance model achieves the Cramér-Rao lower bound. Thus, this covariance model is used for the work presented here, which is denoted by R_i^{INSTR} .

The error that exists in catalog or reference vectors, \mathbf{r}_i , is due to the orbit determination process that generated the catalog. The covariance of the orbit determination process provides critical information into the accuracy of the reference vectors in the catalog. In the case of decentralized orbit determination, the error of the reference vectors is generally greater than that of reference vectors created by centralized orbit determination methods. To compare the performance of the data association methods, two separate catalogs are created. One has errors representative of decentralized orbit determination, while the other possess errors which correspond to centralized orbit determination. It is assumed that the error-covariance of the i^{th} RSO estimate, denoted by $\hat{\mathbf{r}}_i^{\text{RSO}}$ is given by R_i^{RSO} . The vector \mathbf{r}_i can be rewritten as

$$\mathbf{r}_i = \frac{\mathbf{r}_i^{\text{RSO}} - \mathbf{r}^{\text{INSTR}}}{\|\mathbf{r}_i^{\text{RSO}} - \mathbf{r}^{\text{INSTR}}\|} \quad (18)$$

Its corresponding estimate is computed by

$$\hat{\mathbf{r}}_i = \frac{\hat{\mathbf{r}}_i^{\text{RSO}} - \mathbf{r}^{\text{INSTR}}}{\|\hat{\mathbf{r}}_i^{\text{RSO}} - \mathbf{r}^{\text{INSTR}}\|} \quad (19)$$

Taking the partial of Eq. (18) with respect to $\mathbf{r}_i^{\text{RSO}}$ gives

$$\mathcal{J}_i \equiv \frac{\partial \mathbf{r}_i}{\partial \mathbf{r}_i^{\text{RSO}}} = \frac{1}{\|\mathbf{r}_i^{\text{RSO}} - \mathbf{r}_i^{\text{INSTR}}\|} I_{3 \times 3} - \frac{(\mathbf{r}_i^{\text{RSO}} - \mathbf{r}_i^{\text{INSTR}})(\mathbf{r}_i^{\text{RSO}} - \mathbf{r}_i^{\text{INSTR}})^T}{\|\mathbf{r}_i^{\text{RSO}} - \mathbf{r}_i^{\text{INSTR}}\|^3} \quad (20)$$

Note that $\mathbf{r}^{\text{INSTR}}$ is constant and is assumed to be well known. It is assumed here that the current $\tilde{\mathbf{b}}_i$ is not used to determine $\hat{\mathbf{r}}_i^{\text{RSO}}$, so that no correlations exist between the estimate and the measurement. This is practically true because the RSO estimates are obtained by propagating the dynamics model along with its error-covariance from a previous time to the time of the instrument sighting. The error due to the uncertainty of the catalog estimated position is given by

$$R_i^{\text{EST}} = A \mathcal{J}_i R_i^{\text{RSO}} \mathcal{J}_i^T A^T \quad (21)$$

Therefore, since the errors between the focal plane and RSO positions are uncorrelated the total covariance accounting for both errors is simply given by

$$R_i = R_i^{\text{INSTR}} + R_i^{\text{EST}} \quad (22)$$

The attitude matrix is used to map the RSO covariance into the instrument coordinate system. Also, note that R_i contains true values of the focal plane observations and true values of the RSO position. These can be replaced with their corresponding measurements or estimates, which leads to second-order error effects in the computation of R_i .

PLANAR TRIANGLE METHOD

The planar triangular method and the spherical triangular methods (STM) are both pattern recognition algorithms initially applied for star identification. These methods are extensions to the popular angle method, which requires two vectors while the STM and PTM require at least three vectors. The novelty lies in the fact that the STM and PTM require less pivoting, and provide a more consistent solution when compared to the angle method for pattern recognition. In this paper, details about the PTM are shown. Details of the STM can be found in Ref. 18. For a complete derivation of the PTM refer to Ref. 10. It has been determined in Ref. 10 that the PTM yields similar performance to that of the STM. Therefore, the PTM is preferred over STM due to reduced complexity and computational cost. The PTM requires that there be at least three objects present in the FOV. Again, it will be necessary to introduce pivoting with the PTM to reduce multiple solutions.

The PTM works on an elementary concept of pattern recognition, i.e. pattern matching for data association of RSOs. The PTM uses the objects present in the FOV to form triangles from which the area and polar moment of the triangles are then calculated. The catalog is then searched for matching areas and polar moments. If multiple matches are found, then one of the vertices of the triangle is pivoted using another star. This process is continued until a single solution can be reached. For the purpose of matching objects in the FOV with that of the ones present in the catalog, the PTM exploits information using some simple geometrical properties of triangles.

The two properties used by the PTM to identify the objects in the FOV are area and polar moment of the planar triangles. The area of the planar triangle can be given by the Heron's formula.¹⁰ Given three unit vectors pointing toward three space objects, denoted by $\tilde{\mathbf{b}}_1$, $\tilde{\mathbf{b}}_2$ and $\tilde{\mathbf{b}}_3$, the area of a planar triangle is given by

$$\mathcal{A} = \sqrt{s(s-a)(s-b)(s-c)} \quad (23)$$

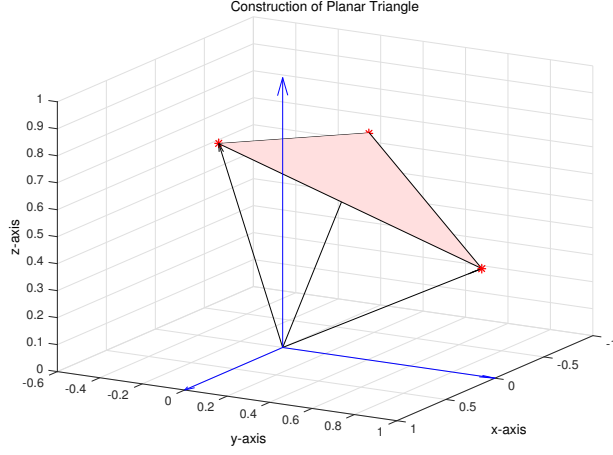


Figure 2. Planar Triangles Formed with Three Objects

where

$$s = \frac{1}{2}(a + b + c) \quad (24a)$$

$$a = \|\tilde{\mathbf{b}}_1 - \tilde{\mathbf{b}}_2\| \quad (24b)$$

$$b = \|\tilde{\mathbf{b}}_2 - \tilde{\mathbf{b}}_3\| \quad (24c)$$

$$c = \|\tilde{\mathbf{b}}_1 - \tilde{\mathbf{b}}_3\| \quad (24d)$$

A depiction of the planar triangle between three unit vectors is shown in Figure 2. In practice, the three unit position vectors contain sensor error. Therefore, an expression for the standard deviation of the planar triangle area is desired. Since Eq. (23) is nonlinear, a linearization technique, similar to how Eq. (17) is derived, is used to extract the variance of the area.

To compute this variance the following 1×9 partial derivative matrix is evaluated:

$$H = [\mathbf{h}_1^T \quad \mathbf{h}_2^T \quad \mathbf{h}_3^T] \quad (25)$$

where

$$\mathbf{h}_1^T \equiv \frac{\partial \mathcal{A}}{\partial a} \frac{\partial a}{\partial \mathbf{b}_1} + \frac{\partial \mathcal{A}}{\partial c} \frac{\partial c}{\partial \mathbf{b}_1} \quad (26a)$$

$$\mathbf{h}_2^T \equiv \frac{\partial \mathcal{A}}{\partial a} \frac{\partial a}{\partial \mathbf{b}_2} + \frac{\partial \mathcal{A}}{\partial b} \frac{\partial b}{\partial \mathbf{b}_2} \quad (26b)$$

$$\mathbf{h}_3^T \equiv \frac{\partial \mathcal{A}}{\partial b} \frac{\partial b}{\partial \mathbf{b}_3} + \frac{\partial \mathcal{A}}{\partial c} \frac{\partial c}{\partial \mathbf{b}_3} \quad (26c)$$

The partials with respect to a , b and c are given by

$$\frac{\partial \mathcal{A}}{\partial a} = \frac{u_1 - u_2 + u_3 + u_4}{4\mathcal{A}} \quad (27a)$$

$$\frac{\partial \mathcal{A}}{\partial b} = \frac{u_1 + u_2 - u_3 + u_4}{4\mathcal{A}} \quad (27b)$$

$$\frac{\partial \mathcal{A}}{\partial c} = \frac{u_1 + u_2 + u_3 - u_4}{4\mathcal{A}} \quad (27c)$$

where

$$u_1 = (s - a)(s - b)(s - c) \quad (28a)$$

$$u_2 = s(s - b)(s - c) \quad (28b)$$

$$u_3 = s(s - a)(s - c) \quad (28c)$$

$$u_4 = s(s - a)(s - b) \quad (28d)$$

The partials with respect to \mathbf{b}_1 , \mathbf{b}_2 and \mathbf{b}_3 are given by

$$\frac{\partial a}{\partial \mathbf{b}_1} = (\mathbf{b}_1 - \mathbf{b}_2)^T / a, \quad \frac{\partial a}{\partial \mathbf{b}_2} = -\frac{\partial a}{\partial \mathbf{b}_1} \quad (29a)$$

$$\frac{\partial b}{\partial \mathbf{b}_2} = (\mathbf{b}_2 - \mathbf{b}_3)^T / b, \quad \frac{\partial b}{\partial \mathbf{b}_3} = -\frac{\partial b}{\partial \mathbf{b}_2} \quad (29b)$$

$$\frac{\partial c}{\partial \mathbf{b}_1} = (\mathbf{b}_1 - \mathbf{b}_3)^T / c, \quad \frac{\partial c}{\partial \mathbf{b}_3} = -\frac{\partial c}{\partial \mathbf{b}_1} \quad (29c)$$

The variance of the area, denoted by $\sigma_{\mathcal{A}}^2$, is given by

$$\sigma_{\mathcal{A}}^2 = H R H^T \quad (30)$$

where

$$R \equiv \begin{bmatrix} R_1 & 0_{3 \times 3} & 0_{3 \times 3} \\ 0_{3 \times 3} & R_2 & 0_{3 \times 3} \\ 0_{3 \times 3} & 0_{3 \times 3} & R_3 \end{bmatrix} \quad (31)$$

where $0_{3 \times 3}$ denotes a 3×3 matrix of zeros and R_1 , R_2 and R_3 are given by Eq. (22). Note that the matrices H and R are evaluated at the respective true values; however, replacing the true values with the measured ones leads to second-order errors that are negligible. Since the standard deviation, $\sigma_{\mathcal{A}}$, is derived analytically, the bounds over which the true area is likely to exist can be determined precisely to within any prescribed confidence level, no matter the shape or size of the planar triangle.

The triangular polar moment of inertia is introduced as a supplemental screening property to the planar triangle area. If two planar triangles have the same area, then their polar moments are most likely different. The reverse is also true; if two planar triangles have the same polar moments, then it is likely that their areas are not equal. The polar moment of inertia property helps further differentiate possible triangle combinations. The polar moment of inertia the planar triangle is given by

$$\mathcal{J} = \mathcal{A}(a^2 + b^2 + c^2)/36 \quad (32)$$

As with the area, the variance of the polar moment of inertia can also be derived in closed form. To compute this quantity the following 1×9 partial derivative matrix is evaluated:

$$\bar{H} = [\bar{\mathbf{h}}_1^T \quad \bar{\mathbf{h}}_2^T \quad \bar{\mathbf{h}}_3^T] \quad (33)$$

where

$$\bar{\mathbf{h}}_1^T \equiv \frac{\partial \mathcal{J}}{\partial a} \frac{\partial a}{\partial \mathbf{b}_1} + \frac{\partial \mathcal{J}}{\partial c} \frac{\partial c}{\partial \mathbf{b}_1} + \frac{\partial \mathcal{J}}{\partial \mathcal{A}} \mathbf{h}_1^T \quad (34a)$$

$$\bar{\mathbf{h}}_2^T \equiv \frac{\partial \mathcal{J}}{\partial a} \frac{\partial a}{\partial \mathbf{b}_2} + \frac{\partial \mathcal{J}}{\partial b} \frac{\partial b}{\partial \mathbf{b}_2} + \frac{\partial \mathcal{J}}{\partial \mathcal{A}} \mathbf{h}_2^T \quad (34b)$$

$$\bar{\mathbf{h}}_3^T \equiv \frac{\partial \mathcal{J}}{\partial b} \frac{\partial b}{\partial \mathbf{b}_3} + \frac{\partial \mathcal{J}}{\partial c} \frac{\partial c}{\partial \mathbf{b}_3} + \frac{\partial \mathcal{J}}{\partial \mathcal{A}} \mathbf{h}_3^T \quad (34c)$$

with

$$\frac{\partial \mathcal{J}}{\partial a} = \mathcal{A} a/18, \quad \frac{\partial \mathcal{J}}{\partial b} = \mathcal{A} b/18, \quad \frac{\partial \mathcal{J}}{\partial c} = \mathcal{A} c/18 \quad (35a)$$

$$\frac{\partial \mathcal{J}}{\partial \mathcal{A}} = (a^2 + b^2 + c^2)/36 \quad (35b)$$

All other quantities in Eq. (34) are given from the area variance calculations. The variance of the polar moment of inertia, denoted by $\sigma_{\mathcal{J}}^2$, is given by

$$\sigma_{\mathcal{J}}^2 = \bar{H} R \bar{H}^T \quad (36)$$

As with the area variance, the true values are replaced with the respective measured polar moment of inertia.

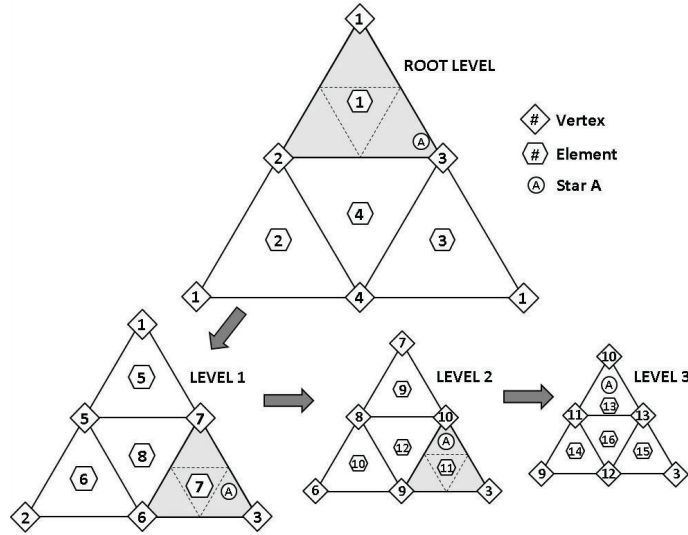


Figure 3. Flattened Spherical Quad-Tree Structure

Planar Triangle Catalog

It is necessary to organize the planar triangle catalog in an efficient manner to help reduce search and creation time. This is especially important because, unlike stars, RSO catalogs are updated frequently (sometimes daily). Therefore, a new planar triangle catalog will need to be created once an RSO catalog is made available. In order to make the catalog easily accessible, a spherical quad-tree structure is used. The spherical quad-tree structure is similar to a traditional quad-tree structure except it uses spherical triangles instead of square quadrants as the element type. The traditional quad-tree is presented in detail in Ref. 18. A spherical quad-tree structure is a multi-level apportioned spherical triangle that enables objects to be associated based on their location within that spherical triangle. If the spherical triangle is flattened in 2-D space, then it would somewhat resemble the triangular structure shown in Figure 3. The spherical triangle is divided into four labeled elements in each of its three levels. Also, each individual element is assigned three labeled vertices. During the spherical quad-tree build, each object is assigned to a spherical triangle and the associated elements based on its location in the celestial sphere. The elements and vertices are the parameters used to locate a particular object in the structure. There are four spherical triangles

that create a spherical tetrahedron that spans the entire celestial sphere. To further simplify the search, only the objects within the specified FOV are considered. Therefore, any object outside this boundary is omitted from the search.

During a search it is not immediately known where each object is located since there are a significant number of them cataloged. To clarify the search process, an example will be presented. Assume that any object in space, denoted as star A in Figure 3, is the only object cataloged, and it is located inside root (top level) – element 1, level 1 – element 7, level 2 – element 11, and level 3 – element 13. Now, suppose measurements are taken and the measured angle lies within a boundary of the spherical triangle, say the lower right of element 1. Considering more levels, the measured angle is determined to lie within element 13. Since star A is contained in element 13, star A is the measured object. If the measured angle lies within a different boundary and other objects are cataloged, then a different object may be identified. Clearly, it is necessary to define multiple levels in order to obtain a sufficient amount of precision when the number of objects is large. The benefit of the spherical quad-tree structure is that once it is created, an object can be identified without using any information about the unit position vector of the object.

The spherical quad-tree is an efficient way to store information, but an optimal organization of the catalog is desired. If the catalog can be organized in such a way that it follows a mathematical equation, then it would be simple to find a particular property in the catalog. For example, if it is determined that the planar triangle area is within a certain boundary, then a search of the catalog for that boundary would be required. If the catalog is not organized appropriately, then it would result in a search spanning the majority of the catalog. Since the catalog can be quite extensive, this would lead to a high computation cost. To resolve this issue the k -vector approach¹⁹ is used. For object pattern recognition, if the area of each pair of objects is plotted against its location in the catalog, then a line can be drawn connecting the first and last pair of objects. The equation of this line can be used in association with the generated k -vector to locate where in the catalog a particular pair of objects with a given angle is located. This greatly reduces the computational burden since the object pattern search algorithm requires a search of the pairs of objects only within a measurement uncertainty region, not a search of the entire catalog. For the planar triangle approach a parabolic k -vector is constructed because it is the best relationship between the planar triangle identifier and the planar triangle area. If a certain planar triangle area is desired, then the k -vector will quickly provide the associated planar triangle identifier.

Planar Triangle Pivot

If several objects are within the FOV, then it is likely that there can be multiple solutions to the search. To reduce and ultimately eliminate multiple solutions, planar triangle pivoting is leveraged. The method for pivoting planar triangles is similar to the method for pivoting angles using two objects. A planar triangle is made from three objects in the FOV, and its area and polar moment of inertia are calculated. A range over which the true area and polar moment of inertia exist are calculated using the standard deviations for each. Going through the catalog, triangles that have an area and polar moment that fit within the bounds calculated for the triangle in the FOV are sought. Ideally, only one possible solution exists, but this is typically unlikely. When more than one solution exists, a pivot is performed. Another planar triangle is made from the objects in the FOV such that there are two objects in common with the first triangle, as shown in Figure 4. A list of possible solutions is made, and then the solutions between the first planar triangle and second planar triangle are compared. Any solution in each list that does not have two objects in common with at least

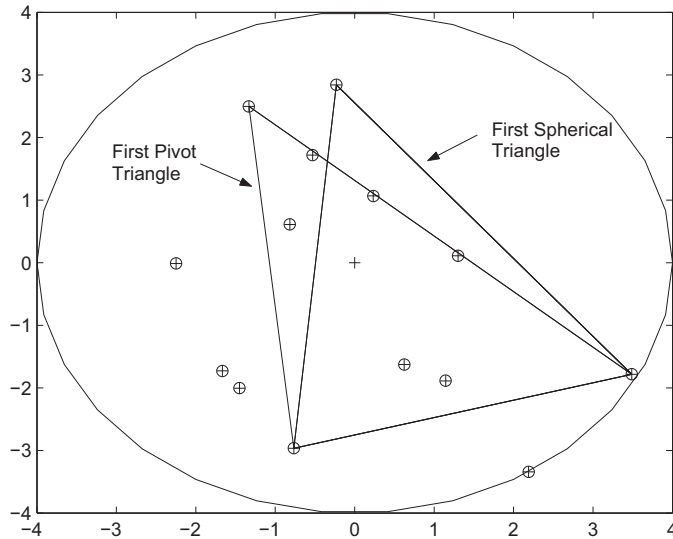


Figure 4. Pivoting within Field of View

one solution in the other lists is discarded. After the comparison is made, if more than one solution exists, then another pivot is made. Pivoting continues until either a single solution is found or the pivoting limit has been met. Pivoting such that only one object is shared between the first and second planar triangles can be done, but would be less effective. The number of triangles that are likely to share one object is greater than two, so the solution would require a greater number of pivots.

Also considering false objects and highly cluttered object patterns, the pivoting order would ideally pivot away from objects that are uncertain. This concept becomes feasible with the addition of the gating method results. Careful ordering of the pivoting of the objects in the FOV allows the PTM to strategically pick the next object to pivot.

ORBIT DETERMINATION

Given the nonlinear nature of space object dynamics, a nonlinear observer is required to handle orbit determination tasks. An Unscented Kalman Filter (UKF) is chosen for the nonlinear estimation because of its accuracy and implementation with nonlinear systems. The errors in orbit determination quickly become non Gaussian which inhibit the accuracy of the UKF which assumes Gaussian error distributions. Future work will include orbit estimation routines that do not require the Gaussian error assumption.

The UKF facilitates nonlinear measurement and dynamics models, which lends itself directly to application of state and parameter estimation in orbit determination applications. The dual, state and parameter estimation functionality will be utilized in this work to estimate states of the observed space object position as well as the ballistic coefficient which is critical to the dynamics of LEO space objects.

DECENTRALIZED VERSUS CENTRALIZED ESTIMATION

Decentralized filtering utilizes individual filters that receive measurements from local sensor nodes and produce independent state estimates. The decentralized filter concept is highlighted in

Figure 5. Each local filter produces an estimate and covariance that result from the local measurements. In this case, the local measurements are optical angles-only observations of space objects. Each local filter is an independent instantiation of the UKF mentioned in previous sections. Therefore, each local measurement site can provide a state estimate independent of the functionality of the other measurement site. The estimates and covariances from the local filters are fed to a fusion node which provides a single, fused state estimate. The number of local filters can be expanded to the number of sensor nodes in the multi-source system.

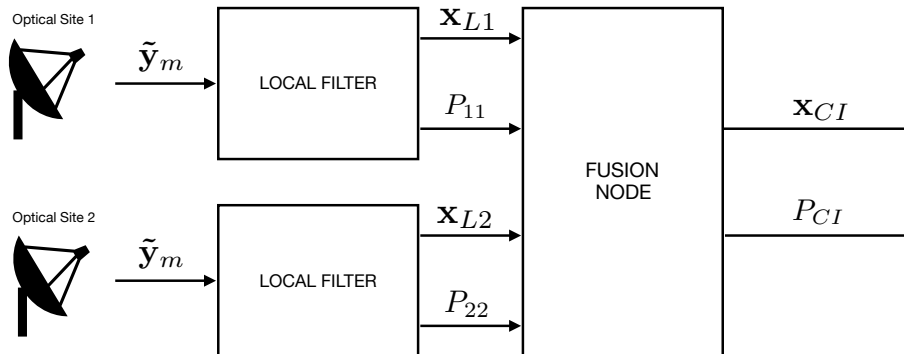


Figure 5. Decentralized Data Fusion Architecture

The method chosen for decentralized node data fusion is the covariance intersection (CI) approach. Covariance intersection²⁰ is a method to combine state estimates and covariance among local, independent filters that maintain consistency. When the cross-covariance is known exactly, i.e. in a centralized solution, the fused estimate's covariance always lies within the intersection of the individual covariances. The form of the estimate and covariance is identical to the standard Kalman filter when independence is given, and it generalizes to a colored-noise Kalman filter when there are known nonzero cross correlations. When the cross-covariance is unknown using a decentralized solution, a consistent estimate still exists when the covariance encloses the intersection region. When cross-covariance information is available, methods exist that provide optimal fusion. However, these methods will not generally provide estimates that match the centralized estimate since they incorporate only information that is posterior to the updates of the estimates being fused.

Consider two estimate pairs $\{\mathbf{x}_{L1}, P_{11}\}$ and $\{\mathbf{x}_{L2}, P_{22}\}$. It is assumed the estimates of \mathbf{x}_{L1} and \mathbf{x}_{L2} are consistent. In an optimal filter, the cross covariance is incorporated naturally into the state covariance computation. This information is unknown in a decentralized system. To generate a consistent estimate, the state estimates \mathbf{x}_{L1} and \mathbf{x}_{L2} are fused by

$$P_{CI}^{-1} = \omega P_{11}^{-1} + (1 - \omega) P_{22}^{-1} \quad (37a)$$

$$\mathbf{x}_{CI} = P_{CI} [\omega P_{11}^{-1} \mathbf{x}_{L1} + (1 - \omega) P_{22}^{-1} \mathbf{x}_{L2}] \quad (37b)$$

where $\omega \in [0, 1]$ is a scalar weight. Reference 20 proves that the estimate \mathbf{x}_{CI} is consistent for all P_{12} and ω . The weight, ω can be found by an optimization routine that minimizes the trace or determinant of the matrix P_{CI} . The trace and determinant characterizes the size of the Gaussian uncertainty ellipsoid associated with P_{CI} . It is straightforward to apply the CI approach to fuse multiple estimates. The CI algorithm closely resembles an electrical resistance calculation within

a parallel architecture. Given a set of M estimates $\{\hat{x}_1, \hat{x}_2, \dots, \hat{x}_M\}$ and associated covariances $\{P_1, P_2, \dots, P_M\}$, a consistent estimate is given by

$$P_{CI}^{-1} = \sum_{i=1}^M \omega_i P_i^{-1} \quad (38a)$$

$$\hat{x}_{CI} = P_{CI} \sum_{i=1}^M \omega_i P_i^{-1} \hat{x}_i \quad (38b)$$

From a given observation of the simulation, the positional covariance matrices were examined and 2D ellipses were plotted for validation of the CI approach. Figure 6 shows how the CI covariance ellipse resides nearly within the intersection of the Local Filter 1 and Local Filter 2 covariance ellipses. The centralized filter covariance ellipse clearly is well within the intersection of the two local filter covariances. Figure 6 further demonstrates the additional conservatism that exists in the decentralized estimate.

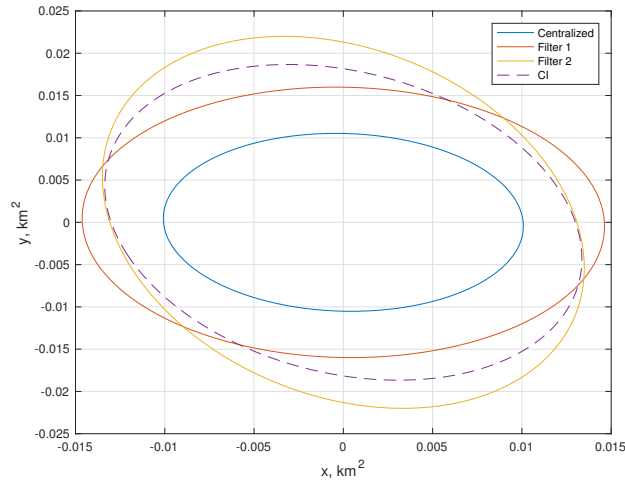


Figure 6. 2D Covariance Ellipse Comparison

Monte Carlo Covariance Analysis

To generate an comprehensive assessment of the accuracy of the centralized and decentralized approaches, a Monte Carlo analysis was performed using the multiple observations of objects with two observation sites. The centralized and decentralized filters were fed the the same measurement data for each Monte Carlo run. The resulting covariance matrices were saved after each run and used to create an understanding of the overall uncertainty performance of the centralized and decentralized orbit determination. Figure 7 illustrates the overlay of the direct terms of the positional covariance matrices for both the centralized and decentralized routines.

The decentralized approach shows a generally larger uncertainty over the simulation time, which corresponds to its overly conservative formulation of the covariance matrix. The resulting covariances at the end of the simulation time are used to add uncertainty to the cataloged values.

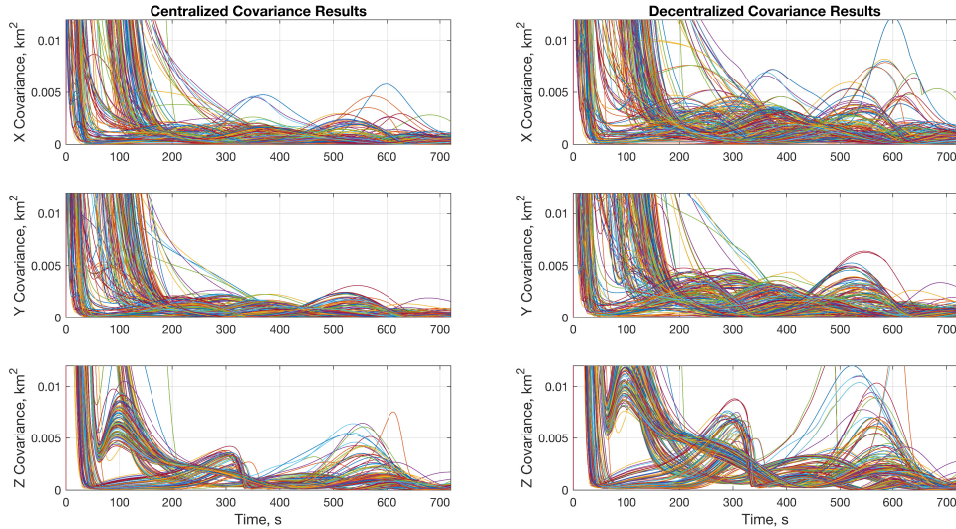


Figure 7. Monte Carlo Covariance Results

TRADITIONAL DATA ASSOCIATION METHODS

Nearest Neighbor (NN) is the simplest data association algorithm, used for single target tracking. When multiple measurements fall within a target's validation gate, the one that is closest with respect to a predefined distance measure is assumed to come from that target. Sometimes called the optimal assignment approach, global nearest neighbor (GNN) is the multi-target version of the NN approach. Instead of minimizing a single distance, GNN looks to minimize a global distance measure. Two assumptions are made: 1) each measurement can only be associated to one track, and 2) each track can only be associated with one measurement. The primary advantage of the GNN algorithm is that its computational cost does not increase rapidly as the number of targets increases. The disadvantage of this algorithm is that track initiation must be performed separately. Reference 21 identifies two classes of track initiation techniques: sequential and batch. The former is preferred for low-clutter environments, while the latter is used for high-clutter environments. The primary difference between the two is that batch techniques are generally slower and more computationally expensive.

Given the highly cluttered field of view of clustered orbital objects, there is a high likelihood of multiple tracks existing in a single gate. For this reason, a GNN approach is used as the data association method for gating. A simple example of a gating method is that of a house with an automatic gate that opens only when the identity of the person at the gate can be verified. However, if the identity cannot be verified, then the person does not have access. Similarly, validation gates do not let the measurement be associated with the track if the measurement does not pass the gate provided by the truth and assumed uncertainty. A gate is formed about the predicted measurement, and all observations that fall within the gate are considered for the track update. The measurement-to-track assignment is solved by way of Munkres Algorithm.

Elliptical Gates

The Mahalanobis distance is synonymous to the ellipsoidal gate. This is a statistical tool used to measure the distance between points in multivariate data. Mahalanobis distance measure is also the distance between a point P and a distribution D . The Mahalanobis distance was originally developed for use with multivariate normal distributed data. A prediction ellipse is a region for predicting the location of a new observation under the assumption that the population is bivariate normal. For example, an 80% prediction ellipse indicates a region that would contain about 80% of the new samples that are drawn from a bivariate normal population with mean and covariance matrices that are equal to the sample estimates. The Mahalanobis distance is also said to be the simple Euclidean distance, which takes into account the covariance of the data. If the covariance of the data is an identity matrix, then the Mahalanobis distance is equivalent to the Euclidean distance. The Mahalanobis distance measure used in this work is mathematically written as: A ellipsoid with center at \mathbf{v} is defined by solutions to \mathbf{x} of the equation

$$(\mathbf{x} - \mathbf{v})^T Z (\mathbf{x} - \mathbf{v}) = 1 \quad (39)$$

where Z is a positive definite matrix. The equation of an ellipse given by Eq. (39) and the Mahalanobis distance are clearly identical in form, and hence the Mahalanobis distance is often referred to as either *elliptical gates* or *ellipsoidal gates*.

The Mahalanobis distance is a powerful method for assessing a measured sample set deviation from expected values based on statistical information about the measurement distribution. This is precisely the RSO data association problem, because it is desired to see how similar a point in space is to all true points in the catalog. Unlike the Euclidean distance the Mahalanobis distance takes into account the following facts:

- It accounts for the fact that the variance is different in each direction;
- It accounts for the covariance between variables;
- It reduces to the Euclidean distance for uncorrelated variables and unit variance.

The Mahalanobis distance takes into account factors such as uncertainty and correlations between measurements. Therefore it is an effective tool to solve the RSO data association problem. It will also be shown that elliptical gates can be used to increase the performance of the PTM. This distance can be combined with algorithms such as the GNN to associate closest neighbors in a multivariate data set. The GNN maintains the single most likely hypothesis. The fundamental concept of the GNN is to associate the most likely assignment of an measurement to its existing estimate across all measurements.

The GNN algorithm can be used with various types of distance measurements (Euclidean, city block, Chebyshev, etc.). The most popular among these is the Mahalanobis distance or the ellipsoidal gate described in this section. The gate can be written in general by

$$G_r = \{\mathbf{z} : D(\mathbf{z}) \leq \gamma\} \quad (40)$$

where $D(\mathbf{z})$ is the distance measure. For the RSO association problem the Mahalanobis distance is used as the distance measure. Also, \mathbf{z} is the estimate, which is determined by propagating the state model of the target forward to the observation time.

Optimal Assignment Problem

After all the possible tracks and measurements are screened via elliptical gating, strategic selection of the lowest cost association is required to address situations where multiple tracks exist within a single elliptical gate. The situation described is solved by an optimal assignment solution. The method chosen for the optimal assignment problem is Munkres algorithm.⁹ Figure 8 illustrates the possibility of multiple tracks passing the elliptical gate for a single observation, where T1 and T2 are possible tracks and M is the observed or measured object.

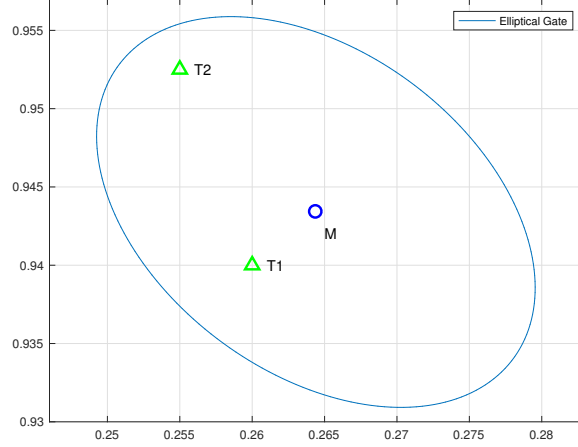


Figure 8. Multiple Track Within Elliptical Gate

The assignment matrix is populated with the Mahalanobis distance values for all the measurement-track combinations that passed the elliptical gate threshold. By populating the assignment matrix with the Mahalanobis distances that passed the elliptical gate, the Munkres assignment algorithm has fewer values to search for the minimum cost. This significantly reduces the computational cost of the Munkres algorithm implementation. The object catalog contains 4000 objects and the field of view is often populated with more than 15 objects at a time, therefore Munkres Algorithm would have to search through a 15×4000 matrix to determine the minimum cost solution. Allowing the gate threshold to screen unlikely solutions reduces that matrix search significantly. The assignment matrix is given by

$$\text{Assignment Matrix} = \begin{bmatrix} d_{11}^2 & d_{12}^2 & d_{13}^2 & \dots & d_{1n}^2 \\ d_{21}^2 & d_{22}^2 & d_{23}^2 & \dots & d_{2n}^2 \\ \vdots & \vdots & \vdots & \ddots & \vdots \\ d_{d1}^2 & d_{d2}^2 & d_{d3}^2 & \dots & d_{dn}^2 \end{bmatrix} \quad (41)$$

where d_{ij}^2 is the squared Mahalanobis distance for the i^{th} measurement and the j^{th} track that passed the elliptical gate of the i^{th} measurement. The square Mahalanobis distance is simply given by

$$d_{ij}^2 = \mathbf{e}_{ij}^T \mathbf{S}_i^{-1} \mathbf{e}_{ij} \quad (42)$$

where \mathbf{e}_{ij} is the residual between the i^{th} measured value and the j^{th} track value and \mathbf{S}_i is the innovations covariance. The goal of Munkres Algorithm is to find the minimum total, or global, cost of the assignment matrix by only selecting one track to one measurement.

The data association via elliptical gating can be implemented via the following description:

1. Compute the Mahalanobis distance from all possible cataloged estimates to all measurements in the FOV;
2. Assemble the assignment matrix with all the tracks which pass the gate threshold;
3. Solve the optimal assignment problem using the Munkres Algorithm.

The association results from gating are fed directly into the PTM algorithm which evaluates the triangle properties of the identified objects against the cataloged values.

SIMULATION RESULTS

To simulate realistic conditions data from the debris field of the 2007 Chinese anti-satellite missile test of the Fengyun 1C satellite is used. This Chinese weather satellite was launched into a Sun-synchronous orbit with a mean altitude of 850 km and an inclination of 98.8 degrees.²² The orbital elements of the 2,000 pieces of debris data for the Fengyun 1C are available on www.celestrak.com. Another set of 2,000 pieces of debris are also simulated to create a sufficient cluttered environment that stresses the data association algorithms.

The chosen site is the Ground-based Electro-Optical Deep Space Surveillance (GEODSS) instrument, which is located at the White Sands Missile Range in New Mexico. The location of the telescope is 32.82° latitude, -106.66° longitude and 1.250 (km) altitude. The second observation site is synthetically placed near the GEODSS instrument to simplify selection of objects which are shared in both sensor's FOVs. The simulated objects are normally distributed about the specific object in the Fengyun 1C debris field that has the smallest separation angle with respect to the normal vector of the site at a specific time. This provides a distribution of 2,000 simulated objects in which the majority are within the view of the site. In total, there are 4,000 RSOs that are cataloged and roughly 2,000 of those are in view of the site.

Simulated objects in ECI coordinates are shown in Figure 9. The ECI initial debris data are then propagated to obtain an instance of time in which there is an acceptable amount of debris visible to the site. Then the debris is converted to the ECEF coordinate system. To see RSOs in the FOV, transformations from ECEF to ENU to the INSTR frame are required. The reader is recommended to review Ref. 1 (chapter 5), for details of the simulations required to generate the RSO.

Filter results of the position errors of the fused estimates are comparable between the centralized and decentralized cases. Results from a simulated orbit determination case are plotted below in Figure 10. Errors from one object in the field of view are plotted. The centralized and decentralized cases have reasonably similar performance with the decentralized case showing larger uncertainty during the simulation time.

From the local filters of the decentralized estimation approach, state estimate accuracy can be assessed. Figure 11 illustrates the error and associated 3σ bounds of the estimate from each of the local filters. Compared to Figure 10, which contained errors from the fused estimates, the local estimates show greater error and uncertainty, which is to be expected as they do not take advantage of the measurement information of the opposing sensor node.

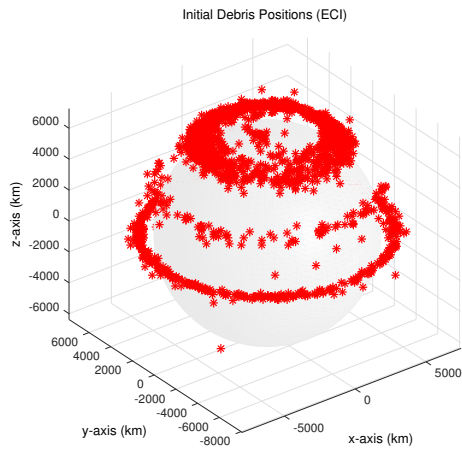


Figure 9. Debris in ECI Coordinate System

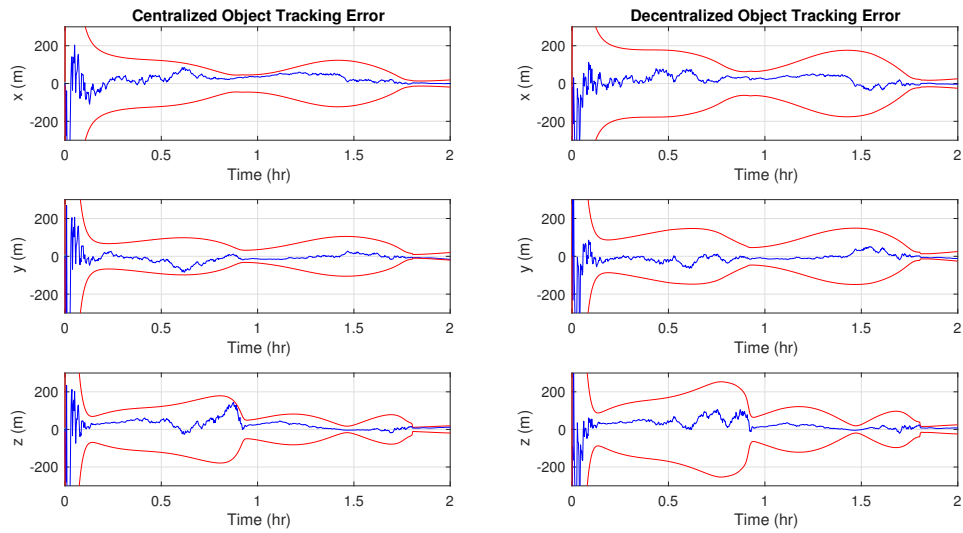


Figure 10. Fused Filter Errors with Centralized *left* and Decentralized *right* Methods

Planar Triangle Method Algorithm

The PTM code execution can be seen in Ref. 10. However a broad overview of the steps can be given as follows:

1. Create the spherical quad-tree structure;
2. Catalog planar triangles;
3. Add planar triangle properties;
4. Sort planar triangles;
5. Run the pattern recognition algorithm in a Monte Carlo regime.

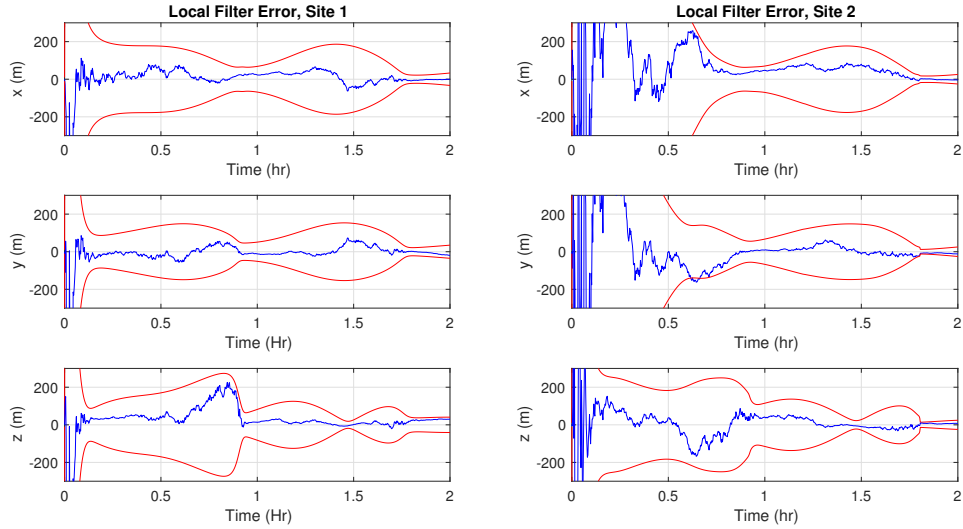


Figure 11. Local Filter Errors for Site 1 *left* and Site 2 *right*

The first step in the PTM code execution is to create a multi-level spherical quad-tree structure. Then, based on an RSO's position data, it is stored within that structure. Once all RSOs have been assigned a position in the tree structure, the planar triangle properties are computed and associated with that tree structure location. To increase efficiency further, a binary tree is implemented to sort the planar triangle properties according to the value of the planar triangle area. The ultimate goal is to provide an efficient storing mechanism that can be used to quickly associate an RSO based on planar triangle area and polar moment.

Once the storing mechanism (steps 1-4) has been constructed, it can now be used to compare focal-plane observations of RSOs from the catalog. Several Monte Carlo runs are executed to test the PTM. At each iteration, a random telescope boresight is generated, and an associated random INSTR frame is constructed. From this INSTR frame, all RSOs within the FOV are provided as inputs to the pattern recognition algorithm. This sequence is repeated many times in order to accumulate a large result set. A representation of the pattern recognition algorithm is as follows:

for $i = 1$ to number of desired iterations **do**

- Compute random boresight vector;
- Compute random INSTR frame with t_z aligned with boresight vector;
- Determine RSOs in FOV;
- Perform ENU to INSTR coordinate system transformation;
- Compute focal-plane observations;
- Add sensor error to focal-plane observations;
- Compute measured RSO position vectors with both measurement and sensor error;

- Compute planar triangle properties;
- Compute area variance;
- Compute polar moment variance;
- Compare computed values with catalog and determine matching RSOs.

The first step in the algorithm is to compute a random boresight vector. This represents a random telescope boresight, which is restricted to the physical attributes of the telescope. The telescope is restricted to an elevation angle of 20 degrees above the horizon and an azimuth angle that spans the entire plane. Therefore the random boresight vectors are uniformly distributed within these boundaries. The random boresight vector is computed by

$$\theta_{\text{elev}} = \frac{\pi}{9} + \left[\frac{\pi}{2} - \frac{\pi}{9} \right] \text{rand}(1) \quad (43a)$$

$$\psi_{\text{az}} = 2\pi \text{rand}(1) \quad (43b)$$

$$\mathbf{r}_b = \begin{bmatrix} \cos(\theta_{\text{elev}}) \cos(\psi_{\text{az}}) \\ \cos(\theta_{\text{elev}}) \sin(\psi_{\text{az}}) \\ \sin(\psi_{\text{az}}) \end{bmatrix} \quad (43c)$$

In the above equation, θ_{elev} and ψ_{az} are the elevation and azimuth angles, respectively. The function `rand` is uniform random number generator. The random INSTR frame is then constructed with the \mathbf{t}_z axis aligned with the current boresight vector.

The INSTR frame is constructed by:

$$\mathbf{t}_z = \mathbf{r}_b \quad (44a)$$

$$\mathbf{t}'_y = \mathbf{t}_z \times \mathbf{r}'_b \quad (44b)$$

$$\mathbf{t}_y = \frac{\mathbf{t}_z \times \mathbf{t}'_y}{\|\mathbf{t}_z \times \mathbf{t}'_y\|} \quad (44c)$$

$$\mathbf{t}_z = \frac{\mathbf{t}_y \times \mathbf{t}_z}{\|\mathbf{t}_y \times \mathbf{t}_z\|} \quad (44d)$$

where \mathbf{r}'_b is a separate random vector generated from Eq. (43c), and \mathbf{t}'_y is a temporary y -axis used to generate the orthogonality condition between \mathbf{t}_z and \mathbf{t}_y . The specific orientation of the \mathbf{t}_{xy} plane is not significant as long as \mathbf{t}_z is along the boresight vector. The instrument is assumed to have a 6 degree FOV, which is represented by a plane at the end point of the random boresight vector. The condition for an object to be within the FOV is given by

$$\arccos(\mathbf{r}^{\text{RSO}} \cdot \mathbf{r}_b) \leq \frac{3\pi}{180} \quad (45)$$

Execution of Gating-Assisted PTM

For the purpose of simulation 1,000 random boresight vectors are generated for both the centralized and decentralized cases. The RSOs in the FOV for each boresight vector are calculated, and when the RSOs in FOV are more than the minimum number desired, the PTM is executed. An illustration of the random boresight vectors computed with the debris can be seen in Figure 12, which

gives a clear understanding of how the boresight vectors are generated, and also helps to visualize the RSOs that are within the FOV. In Figure 12 the red dots are the debris in space. The blue straight lines pointing up towards the debris are the boresight vectors of the telescope. The blue lines at the base of the boresight vectors show the other two axes of each boresight vector. The blue circular head on top of each boresight vector is the FOV for that particular telescope boresight, and the light pink triangles are the planar triangles formed between the debris pieces in space. For the purpose of simulations, the variation of the catalog error represents the uncertainty analyzed in the Monte Carlo covariance assessment of the centralized and decentralized methods. The uncertainty built into the catalog values is listed in Table 1. The sensor error was kept constant for each test as the simulation was focused on determining the difference between centralized and decentralized orbit determination.

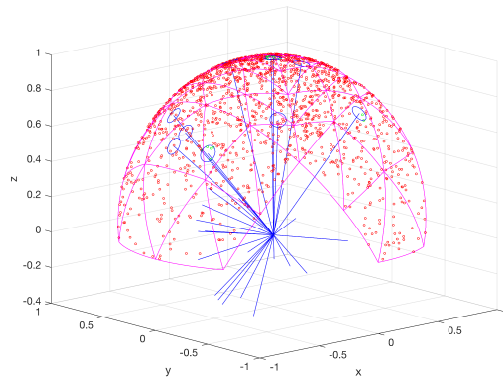


Figure 12. Random Attitude Tests with Debris

Table 1. Estimate Errors

Estimation Type	Centralized	Decentralized
3σ X Estimate Errors (km)	0.1405	0.1926
3σ Y Estimate Errors (km)	0.1199	0.1635
3σ Z Estimate Errors (km)	0.1243	0.1574

The difference between the uncertainty of the centralized estimate and the decentralized estimate is respectable. Greater than a 36% increase in uncertainty is noted between the X and Y components of position errors when comparing the centralized to the decentralized uncertainty. The data association methods used to determine the objects in the field of view is shown to overcome the increase in uncertainty due to decentralized estimation methods.

Gating-Based Data Association

Gating-based data association involves the association of measurements to known true values or tracks, and the sorting of results based on the data association method. As mentioned the data association method for this simulation is the GNN method as executed by the Munkres Algorithm. In order to evaluate the performance of this algorithm with respect to object association, randomly selected FOVs in the aforementioned object measurement and catalog are selected and used as an input to the gating method. Figure 13(a) shows the number of debris objects visible to the ground

site for a representative single run. The Mahalanobis distance between each measured observation and all its true positions are found. Then Munkres algorithm is used to associate the closest measured value to the true debris based on all the tracks that passed the elliptical gate. At the output of each association, a check is performed to see if the associated objects match the true objects. If both the measured and truth are the same, then a correct match is counted and the truth counter is incremented, else a bad/fail counter is incremented. Reference 23 includes detailed performance of gating-only data association.

Cluttering the FOV to Test Gating and PTM

Since the gating method performs exceptionally well in cases where the FOV is very lightly populated with objects,²³ the system is strained for cases where the FOV is very dense, or cluttered with objects. A function is used to artificially add pieces of debris in the FOV. To add closely spaced debris the pairwise distance between each piece of debris in the FOV is taken. The minimum distance in each case is taken and used as the 3σ (standard deviation) to generate three pieces of debris around each already existing debris to populate the FOV, as shown in Figure 13(b). This figure illustrates the cluttering approach used to demonstrate performance of the proposed algorithms.

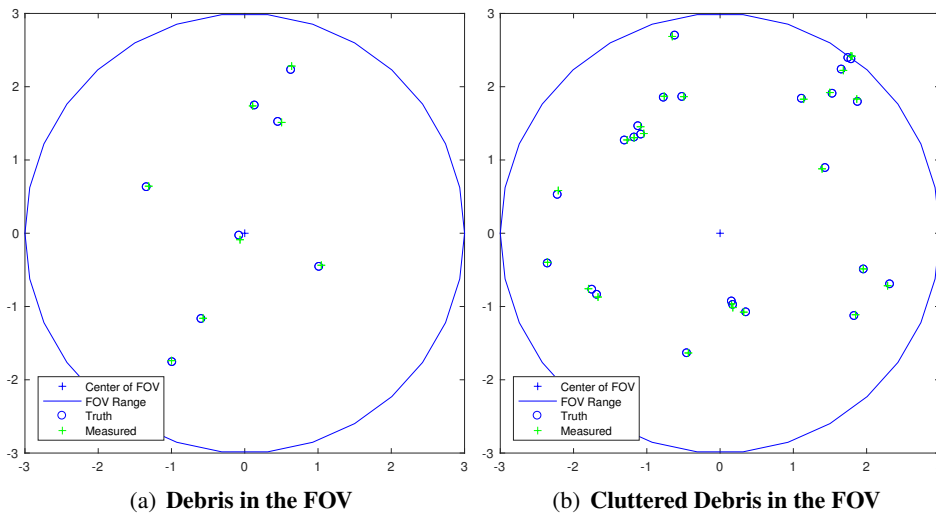


Figure 13. Data Association Performance Comparison, Noise Sensitivity

The cluttering to the FOV is simulated in two different ways. In the first method, the cluttered objects act as false objects that do not exist in the catalog. Here, the gating and PTM algorithms must throw away those objects as not associated with cataloged values. The second method catalogs the clutter objects to create a highly dense cataloged FOV. The data association methods must differentiate between the closely spaced objects to determine the proper association.

GATING-ASSISTED PLANAR TRIANGULAR METHOD

This method couples the working of the PTM and the gating method. First, the gating method is executed as a precursor to the PTM. Here, the gating method is used to associate the measured data to the truth data under varying errors. Once gating data associations are completed, the PTM is executed using the updated track values determined in the gating process.

The pre-processing of the measurement field with the gating data association helps the PTM to compare debris pieces that are already associated to the truth. In the case where the gating process incorrectly matches a measurement to the wrong track, the PTM algorithm has additional criteria in the triangle properties to screen mismatches. The polar moment of inertia provides additional screening criteria to evaluate observations determined in the gating processing. When considering the flexibility to use the pivoting methods, the PTM acts as a robust additional screening method for gating results.

Additional performance can be realized by providing an intelligent pivoting order based on the output of the gating results. If there are sufficient gating-associated objects, then the combinations of associated objects are determined, and then they are sorted based on triangle area. The sorted results are re-organized to follow the traditional pivot method where one object of the triangle is shifted from the first to the next analysis. This approach allows the PTM to use more information yielded from gating to assist in determining precise and robust object association. If more pivots are available, then the objects in the FOV that are not associated by gating can fill out the remainder of the pivots. Along with the updated object vectors, the pre-sorted pivot list is handed over to the traditional PTM algorithm.

The gating-assisted PTM object association method is summarized as follows:

- Perform gating data association with measured objects in the FOV;
- Update measured tracks with associated vectors based on the output of the gating method;
- Determine triangles and planar triangle area based on the combinations of the observations;
- Sort the area of the triangles in descending order;
- Starting with the largest area and smallest combined Mahalanobis distance, re-sort triangles based on pivoting logic used in the PTM approach;
- Using the pivoting list and updated track vectors, execute the PTM algorithm to determine object matches.

Outputting a failed result from the PTM given incorrectly associated objects in the gating pre-processing is almost as good as a correct output from the PTM. By signifying a failure given incorrect observations, the PTM acts as a screen previously unavailable to the gating method alone. Without the PTM addition, the gating method can supply incorrect matches without any additional checks.

By prioritizing the inputs of the PTM with the results of the gating method, notable improvements to the stand-alone performance of both algorithms are realized. The synergistic result of joining these two methods yields improvements than either alone. The PTM benefits from the prioritization of results from gating because it does not have to pivot through uncertain measurements. The gating method benefits from the robustness of the PTM because the PTM can correct and/or reject incorrect associations made from gating. The gating-assisted PTM is also shown to perform well under highly populated false object cases.

Data Association Results

The purpose of this work is to show that the additional uncertainty of the decentralized orbit determination process can be overcome by utilizing a novel data association algorithm consisting of elliptical gating combined with the planar triangle method to associate the measured observations to the truth. Data association algorithm performance was evaluated under a highly challenging measurement environment for both centralized and decentralized catalog error cases.

A comprehensive study has been performed using a cluttered field of view and the novel data association algorithms. The algorithms were evaluated with varying estimate uncertainty corresponding to the results of the Monte Carlo covariance analysis discussed in Section .

The baseline data association method used was the gating-assisted PTM. As described above in Section , the gating-assisted PTM utilizes the gating algorithm as a precursor to the PTM. When this gating method is performed before the PTM, significant robustness to sensor and estimate uncertainty is shown. The results shown in Table 2 demonstrate nearly identical data association performance when comparing centralized to decentralized estimation. The gating-assisted PTM shows an excellent resiliency to estimate uncertainty.

Table 2. Gating-Assisted PTM Performance with Highly Cluttered Field of View

	Success Percentage, Cataloged Objects	
	Centralized	Decentralized
Gating Only	97.9%	97.3%
Gating+PTM	99.8%	99.6%

Table 2 demonstrates that in the cluttered, cataloged case, gating was shown to be quite effective. The addition of the PTM to the gating method provided additional accuracy nearly equivalently for the centralized and decentralized error cases. The screening capability of the gating algorithm significantly enhances the success rate of the output by utilizing the planar triangle properties as well as pivoting. The significant improvement of associated object combinations outputted from the gating-assisted PTM is notable given the harsh cluttering and wide-ranging uncertainty conditions. The gating-assisted PTM is able to provide greater than 99% accuracy across all uncertainty conditions in the cluttered FOV.

To evaluate the performance of the proposed algorithm in yet another challenging environment, the clutter added to the FOV is not cataloged, therefore the clutter acts as false object observations. The false object could be an uncataloged star/object or a sensor malfunction. It is important to note that the approach in this work uses “static” (spatial) observations (i.e. one snapshot in the FOV), unlike “dynamic” (temporal) filtering-based methods. Therefore, actual objects in the FOV can be treated as false objects. Clearly by adding three times the number of false objects than the number of real objects, the simulation case is extremely challenging. The PTM approach alone would unlikely be able to provide any solution given the low probability of selecting real objects out of the FOV, and without using an extraordinarily high pivot limit. But the gating method will help match measurements to existing objects based on the Mahalanobis distance. Results show excellent performance of the gating-assisted PTM in both the centralized and decentralized cases. Table 3 demonstrates the ability of the gating-assisted PTM to overcome significant numbers of false objects and estimate uncertainty to provide the correct object association. The larger uncertainty of the decentralized catalog is handled well by the gating-assisted PTM data association; providing nearly identical performance of that of the centralized catalog. In the false object case, gating clearly

had more trouble identifying the correct objects as compared to the highly cluttered and cataloged FOV.

Table 3. Gating-Assisted PTM Performance with False Objects In Field of View

	Success Percentage, False Objects	
	Centralized	Decentralized
Gating Only	92.2%	89.4%
Gating+PTM	99.7%	99.9%

Not only does the addition of gating-based preconditioning of the observations improve the successful identification rate in the gating-assisted PTM, but it also reduces the number of pivots required in the PTM. Reducing of the number of pivots increases the efficiency of the algorithm and decreases the computational effort as well. Table 4 illustrates the mean and 1σ number of pivots used for the standard PTM and the gating-assisted PTM. Table 4 shows the gating-assisted PTM requires very little pivoting as the gating pre-conditioning helps focus the PTM algorithm towards successful identifications. The additional information provided by the gating preconditioning starts the PTM on observations with higher certainty of association as they have passed the Mahalanobis distance gate. With information on highly certain observations provided from gating, the PTM can accurately associate the observations with very little pivoting.

Table 4. Pivoting Statistics

Test Case	Average Pivots		Standard Dev. Pivots	
	Centralized	Decentralized	Centralized	Decentralized
False Object Clutter	0.320	0.388	0.539	0.490
Cataloged Clutter	0.351	0.4570	0.789	0.590

Data is also presented that describes the gating-assisted PTM algorithm’s response to incorrect identifications from the gating preconditioning. When the gating algorithm incorrectly identified objects in the FOV, the PTM must handle the misinformation. Simulated data shows that the PTM segment of the gating-assisted is able to utilize pivoting to reject incorrect data from gating until a group of three observations match cataloged triangle properties.

CONCLUSIONS

With the success of the data association algorithms presented here, it was shown that the uncertainty of decentralized orbit determination algorithms can be overcome. A hybrid elliptical gating and planar triangle method data association scheme proved to provide robust, accurate associations at a success rate nearly identically for centralized or decentralized estimation. This work extends the concepts of using ellipsoidal validation gates to data association and pattern recognition algorithms such the planar triangle method (PTM). The proposed method of using a ellipsoidal gating as a precursor to the PTM shows significant improvement in accuracy of objects being correctly associated when compared to the PTM or gating method alone in a highly challenging field of view. This method is fairly simple and compact in implementation and is shown to be robust in situations of high uncertainty and cluttered object measurements. The gating-assisted PTM enables the benefits of decentralized estimation and object tracking that are often dismissed because of the lack of state estimate certainty compared to centralized approaches. Implementation of Munkres Algorithm to

solve the optimal assignment problem proved to be an efficient and accurate solution under false object and highly cluttered measurements.

When the gating method is joined with the PTM, a significant improvement in robustness and accuracy is realized. The synergistic effect of combining the two methods removes certain disadvantages of each. The PTM provides additional screening and checking to the gating output data, while the gating output data provides a verified starting point for the PTM to begin its search. The addition of a smart pivoting index as an output of the gating method proves to increase reliability of the PTM.

REFERENCES

- [1] P. E. Silversmith, "Space-Object Identification Using Spatial Pattern Recognition," Master's thesis, University at Buffalo, State University of New York, 2013.
- [2] D. A. Vallado, *Fundamentals of Astrodynamics and Applications*. Torrance, CA: Microcosm Press, 4th ed., 2013.
- [3] K. Hill, K. T. Alfriend, and C. Sabol, "Covariance-based Uncorrelated Track Association," *AIAA/AAS Astrodynamics Specialist Conference and Exhibit*, Honolulu, HI, 2008. AIAA 2008-7211, doi:10.2514/6.2008-7211.
- [4] D. Giza, P. Singla, J. Crassidis, R. Linares, P. Cefola, and K. Hill, "Entropy-Based Space Object Data Association Using an Adaptive Gaussian Sum Filter," *AIAA/AAS Astrodynamics Specialist Conference*, Toronto, ON, Canada, 2010. AIAA 2010-7526, doi:10.2514/6.2010-7526.
- [5] K. J. DeMars, I. I. Hussein, C. Frueh, M. K. Jah, and R. S. Erwin, "Multiple-Object Space Surveillance Tracking Using Finite-Set Statistics," *Journal of Guidance, Control, and Dynamics*, Vol. 38, March 2015, pp. 1741–1756. doi:10.2514/1.G000987.
- [6] Y. Cheng, K. DeMars, and C. Früh, "Gaussian Mixture PHD Filter for Space Object Tracking," *AAS/AIAA Space Flight Mechanics Meeting*, Kauai, HI, 2013. AAS 13-242.
- [7] B. A. Jones and B.-N. Vo, "A Labeled Multi-Bernoulli Filter for Space Object Tracking," *AAS/AIAA Space Flight Mechanics Meeting*, Williamsburg, VA, 2014. AAS 15-413.
- [8] M. J. Holzinger, "Using Magnetometers for Space Object Characterization in Space Situational Awareness Applications," *Journal of Guidance, Control, and Dynamics*, Vol. 37, Sept.-Oct. 2014, pp. 1397–1405. doi:10.2514/1.G000523.
- [9] S. Blackman and R. Popoli, *Design and Analysis of Modern Tracking Systems*. Boston, MA: Artech House, 1999.
- [10] C. L. Cole and J. L. Crassidis, "Fast Star-Pattern Recognition Using Planar Triangles," *Journal of Guidance, Control, and Dynamics*, Vol. 29, Jan.-Feb. 2006, pp. 64–71. doi:10.2514/1.13314.
- [11] H. Schaub and J. L. Junkins, *Analytical Mechanics of Space Systems*. Reston, Virginia: American Institute of Aeronautics and Astronautics, Inc., 2nd ed., 2009.
- [12] F. L. Markley and J. L. Crassidis, *Fundamentals of Spacecraft Attitude Determination and Control*, pp. 382–388. New York, NY: Springer, 2014. doi:10.1007/978-1-4939-0802-8.
- [13] D. L. Light, "Satellite Photogrammetry," *Manual of Photogrammetry* (C. C. Slama, ed.), ch. 17, Falls Church, VA: American Society of Photogrammetry, 4 ed., 1980.
- [14] M. D. Shuster, "Kalman Filtering of Spacecraft Attitude and the QUEST Model," *Journal of the Astronautical Sciences*, Vol. 38, July-Sept. 1990, pp. 377–393.
- [15] M. D. Shuster and S. D. Oh, "Three-Axis Attitude Determination from Vector Observations," *Journal of Guidance and Control*, Vol. 4, No. 1, Jan.-Feb. 1981, pp. 70–77. doi:10.2514/3.19717.
- [16] Y. Cheng, J. L. Crassidis, and F. L. Markley, "Attitude Estimation for Large Field-of-View Sensors," *Journal of the Astronautical Sciences*, Vol. 54, July-Dec. 2006, pp. 433–448.
- [17] J. C. Hinks and J. L. Crassidis, "Covariance Analysis of Maximum Likelihood Attitude Estimation," *The Journal of the Astronautical Sciences*, Vol. 60, No. 2, 2013, pp. 186–210. doi:10.1007/s40295-014-0028-7.
- [18] C. L. Cole, "Fast Star Pattern Recognition Using Spherical Triangles," Master's thesis, University at Buffalo, State University of New York, 2004.
- [19] D. Mortari, "A Fast On-Board Autonomous Attitude Determination System Based on a new Star-ID Technique for a Wide FOV Star Tracker," *AAS/AIAA Space Flight Mechanics Meeting*, Austin, TX, 1996. AAS 96-158.

- [20] S. J. Julier and J. K. Uhlmann, "A non-divergent estimation algorithm in the presence of unknown correlations," *Proceedings of the 1997 American Control Conference (Cat. No.97CH36041)*, Vol. 4, Jun 1997, pp. 2369–2373 vol.4, 10.1109/ACC.1997.609105.
- [21] H. Leung, Z. Hu, and M. Blanchette, "Evaluation of multiple target track initiation techniques in real radar tracking environments," *IEE Proceedings - Radar, Sonar and Navigation*, Vol. 143, Aug. 1996, pp. 246–254. doi:10.1049/ip-rsn:19960404.
- [22] N. L. Johnson, E. Stansbery, J.-C. Liou, M. Horstman, C. Stokely, and D. Whitlock, "The Characteristics and Consequences of the Break-Up of the Fengyun-1C Spacecraft," *Acta Astronautica*, Vol. 63, July-Aug. 2008, pp. 128–135. doi:10.1016/j.actaastro.2007.12.044.
- [23] A. Kalur, S. A. Szklany, and J. L. Crassidis, "Space Object Data Association Using Spatial Pattern Recognition Approaches," *AIAA Guidance, Navigation, and Control Conference*, American Institute of Aeronautics and Astronautics, 2017/01/05 2017.